Equivalence between Fermion-to-Qubit Mappings in two Spatial Dimensions

Yu-An Chen (陳昱安)[1,2,*] and Yijia Xu (许逸葭)[1,3,†]

[1]*Department of Physics, Joint Quantum Institute, and Joint Center for Quantum Information and Computer Science, NIST/University of Maryland, College Park, Maryland 20742, USA*

[2]*Condensed Matter Theory Center, University of Maryland, College Park, Maryland 20742, USA*

[3]*Institute for Physical Science and Technology, University of Maryland, College Park, Maryland 20742, USA*

We argue that all locality-preserving mappings between fermionic observables and Pauli matrices on a two-dimensional lattice can be generated from the exact bosonization in Chen *et al.* [Ann. Phys. (N. Y) 393, 234 (2018)], whose gauge constraints project onto the subspace of the toric code with emergent fermions. Starting from the exact bosonization and applying Clifford finite-depth generalized local unitary transformation, we can achieve all possible fermion-to-qubit mappings (up to the re-pairing of Majorana fermions). In particular, we discover a new supercompact encoding using 1.25 qubits per fermion on the square lattice. We prove the existence of finite-depth quantum circuits to obtain fermion-to-qubit mappings with qubit-fermion ratios $r = 1 + 1/2k$ for positive integers k, utilizing the trivialness of quantum cellular automata in two spatial dimensions. Also, we provide direct constructions of fermion-to-qubit mappings with ratios arbitrarily close to 1. When the ratio reaches 1, the fermion-to-qubit mapping reduces to the one-dimensional Jordan-Wigner transformation along a certain path in the two-dimensional lattice. Finally, we explicitly demonstrate that the Bravyi-Kitaev superfast simulation, the Verstraete-Cirac auxiliary method, Kitaev's exactly solved model, the Majorana loop stabilizer codes, and the compact fermion-to-qubit mapping can all be obtained from the exact bosonization.

I. INTRODUCTION

A fermion-to-qubit mapping is a duality between local even [1] fermionic operators and local products of Pauli matrices. It is well known that any fermionic system in a one-dimensional (1d) lattice can be mapped onto a 1d spin system by the Jordan-Wigner transformation. The Jordan-Wigner transformation can also be applied to systems in higher dimensions by choosing a particular ordering of fermions; however, the mapping becomes highly nonlocal. From both theoretical and practical points of view, mapping local fermionic operators to local spin operators in higher dimensions is an essential topic. In the last two decades, there have been many proposals of fermion-to-qubit mappings for two dimensions [2–10] and three or arbitrary dimensions [11–14]. Beside the qubit degrees of freedom, another approach utilizes Dirac

matrices to achieve a local representation of fermions [15–18]. These mappings play important roles in various topics of modern physics, such as exactly solvable models for topological phases [4,19–23], fermionic quantum simulations [3,5,7,9,11], and quantum error correction [24–29]. In particular, the exact bosonizations in Refs. [2,12,13,16] construct the toric code with fermions in arbitrary dimensions and impose gauge constraints to restrict into the subspace with emergent fermions, which provide an elegant space-time description by the Chern-Simons and the Steenrod square topological action. The space-time pictures for other fermion-to-qubit mappings are not manifest, but the connection of some mappings with the toric code has been pointed out. Whitfield *et al.* [5] indicated that the Verstraete-Cirac auxiliary method [3] can be related to a topological model, and the compact encoding [9] found that the stabilizer is similar to the toric code. Therefore, people should expect that all mappings are closely related.

From the theoretical perspective, since the exact bosonization has the simplest space-time interpretation, it is natural to ask a question: are all fermion-to-qubit mappings in two spatial dimensions "equivalent" to the exact bosonization? First, we define the "equivalence" by finite-depth generalized local unitary (GLU) transformations. Informally, the finite-depth GLU transformation is a

finite-depth quantum circuit with ancilla qubits. We argue that the answer to the above question is "yes" and demonstrate it with examples.

From the practical point of view, fermion-to-qubit mappings are widely used in fermionic quantum simulations of physical systems. For quantum simulations, an important quantity is the qubit-fermion ratio r, the number of qubits to simulate one fermion on average since it is directly related to the total number of fermionic modes encoded in a qubit array. Suppose that we encode n fermionic modes by m qubits; then the qubit-fermion ratio is m/n. On the 2d square lattice, the compact fermion-to-qubit mapping in Ref. [9] has the ratio $r = 1.5$, and Ref. [6] gives a general construction of a fermion-to-qubit mapping with a trade-off between the ratio and the locality of logical operators.

In this work, we focus on lattices in two spatial dimensions. First, we construct a new supercompact fermion-to-qubit mapping with the qubit-fermion ratio $r = 1.25$ on the 2d square lattice. Moreover, we provide a systematic approach to construct various 2d bosonizations by utilizing the ideas of Clifford circuit [30,31] and finite-depth GLU transformations [32,33]. Such an approach provides a new perspective to studying the relationship between different fermion-to-qubit mappings. We find that all the local fermion-to-qubit mappings can be generated from the exact bosonization by finite-depth GLU transformations. In particular, we explicitly show how to obtain the Bravyi-Kitaev superfast (BKSF) encoding, the Verstraete-Cirac mapping, Kitaev's honeycomb model, the Majorana loop stabilizer codes (MLSCs), and the compact fermion-to-qubit mapping.

A. Summary of results

In Sec. II, we first define the crucial theoretical technique: the GLU transformation [32,33]. Then, in Sec. II B, we derive the fermion-to-qubit mapping with ratio $r = 1.5$, which is equivalent to the compact encoding [9]. In Sec. II C, we further improve the ratio to obtain the supercompact fermion-to-qubit mapping with ratio $r = 1.25$. In Sec. II D, we prove that a general construction with ratio

$r = 1 + 1/2k$ can be obtained via a GLU transformation for any positive integer k. The proof utilizes the trivialness of 2d quantum cellular automata (QCA) [34,35]. In Sec. III, we define the equivalence relation between different 2d bosonizations based on finite-depth GLU transformations and argue the equivalence between the exact bosonization and all other fermion-to-qubit mappings. We demonstrate explicit Clifford circuits that convert the exact bosonization to the Bravyi-Kitaev superfast encoding (Sec. III A), the Verstraete-Cirac mapping (Sec. III B), Kitaev's honeycomb model (Sec. III C), the Majorana loop stabilizer codes (Sec. III D), and the Jordan-Wigner transformation (Sec. III E). The characterization and comparison between different fermion-to-qubit mappings is shown in Table I.

An explicit fermion-to-qubit mapping with an arbitrary qubit-fermion ratio is shown in Appendix A. The unitary transformation of the Clifford circuit is provided in Appendix B. In Appendix C, we provide another expression for the supercompact fermion-to-qubit mapping where the fermionic modes are encoded in vertices; such a construction is equivalent to the supercompact mapping in Sec. II C by shifting and re-pairing of Majorana fermions.

II. GENERALIZED LOCAL UNITARY CIRCUITS ON THE EXACT BOSONIZATION

In this section, we describe a systematical way to derive various fermion-to-qubit mappings from the exact bosonization in two spatial dimensions proposed in Ref. [2]. The exact bosonization utilizes the subspace of the toric code with fermionic excitations, which will be shortly reviewed in Sec. II A. We obtain new fermion-to-qubit mappings by applying local unitary operators on the exact bosonization. On the other hand, to include the lattice deformation that could modify the underlying Hilbert space, local unitary operators are insufficient, and the idea of GLU operators is introduced [32,33]. The physical intuition of GLU operators is that we are allowed to add an extra ancilla qubit into the system or remove any single qubit that is unentangled from the rest (forming a tensor

TABLE I. Comparison between fermion-to-qubit mappings on the 2d square lattice.

	Qubit-fermion ratio r	Fermion parity weight	Hopping weight	Stabilizer weight
Verstraete-Cirac mapping [3][a]	2	1	3–4	6
BKSF encoding [11][b]	2	4	2–6	6
Kitaev's honeycomb model [4]	2	2	2–5	6
Exact bosonization [2]	2	4	2–6	6
MLSC [7]	2	3	3–4	4–10
Compact fermion-to-qubit mapping [9]	1.5	1	3	8
Supercompact fermion-to-qubit mapping	1.25	1–2	2–6	12

[a]The graph structure of the auxiliary Hamiltonian is given in Fig. 12 below.
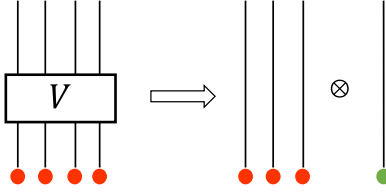[b]The ordering of edges is shown in Fig. 11 below.

FIG. 1. We disentangle the green qubit from others by a local unitary transformation V and then remove this part. This is called a generalized local unitary circuit.

product state), i.e., mapping a state $|\Psi\rangle$ to another state $|\Psi\rangle \otimes |0\rangle$ and vice versa. As shown in Fig. 1, we could apply a unitary operator V making one qubit disentangled from the others, and then remove this qubit without losing any information.

The GLU operators discussed above are for quantum states, which can also be understood for stabilizer codes [36] from the Hamiltonian perspective. Given the Hilbert space formed by N qubits, a stabilizer code is described by a Hamiltonian

$$H_{\text{stabilizer}} = -\sum_{i=1}^{l} S_i \qquad (1)$$

with $l \leq N$ and the stabilizers S_i as functions of Pauli matrices commuting with each other, i.e., $[S_i, S_j] = 0$ for all i, j. The ground states (codewords) are eigenstates of each S_i. If we could find a unitary operator V such that $US_lU^\dagger = Z_N$ (the Pauli Z on the last qubit), all ground states contain an unentangled trivial product state $|0\rangle$ on the last qubit after the basis transformation V. Therefore, we can remove the last qubit from this system without affecting the others.

We use a three-qubit bit-flip repetition code to demonstrate this disentanglement procedure. Consider a three-qubit bit-flip repetition code whose stabilizers are $S_1 = Z_1Z_2$ and $S_2 = Z_2Z_3$; the codewords are

$$|0\rangle_L = |000\rangle, \qquad |1\rangle_L = |111\rangle. \qquad (2)$$

We then apply a Clifford unitary $V = \text{CNOT}_{2\to 3}$ to transform the stabilizers

$$V(Z_1Z_2)V^\dagger = Z_1Z_2, \qquad V(Z_2Z_3)V^\dagger = Z_3. \qquad (3)$$

The second stabilizer Z_2Z_3 is trivialized by disentangler $\text{CNOT}_{2\to 3}$, which indicates that the third physical qubit must be in the $|0\rangle$ state while the first two physical qubits still form the two-qubit repetition code. This fact can also be verified from the state's perspective:

$$\text{CNOT}_{2\to 3} |0\rangle_L = |000\rangle, \qquad \text{CNOT}_{2\to 3} |1\rangle_L = |110\rangle. \quad (4)$$

Here the third physical qubit is always $|0\rangle$ and is disentangled from the rest of the system. Hence we can remove

the third physical qubit and obtain the two-qubit bit-flip repetition code.

On the other hand, the logical operators [37] must be conjugated by the disentangler V, such that they still commute with the transformed stabilizers. Hence, this disentanglement process preserves the algebra in the codespace formed by the codewords. In the above example, the logical operators for codewords in Eq. (2) are

$$X_L = X_1X_2X_3, \qquad Z_L = Z_1, \qquad (5)$$

and are transformed to

$$V(X_1X_2X_3)V^\dagger = X_1X_2, \qquad V(Z_1)V^\dagger = Z_1, \qquad (6)$$

which are the logical operators for the two-qubit repetition code.

Given a fermion-to-qubit mapping represented by a stabilizer code, we disentangle a fraction of physical qubits by choosing specific unitary operators V, i.e., a fraction of stabilizers becoming single Pauli operators after conjugation by V. With the GLU transformation, we can remove the degrees of freedom in the system when they are in a product state. Hence, the qubit-fermion ratio r can be improved by wisely applying finite-depth GLU operators. In this paper, we use finite-depth GLU Clifford circuits since we focus on Pauli stabilizer models. We demonstrate the construction of fermion-to-qubit mappings with the qubit-fermion ratios $r = 1.5$ in Sec. II B and $r = 1.25$ in Sec. II C by conjugating the 2d exact bosonization with certain finite-depth GLU Clifford circuits.

A. Review of the exact bosonization

We review the exact bosonization on the Hilbert space defined in Fig. 2. The elements of vertices, edges, and faces are denoted v, e, f. On each face f of the lattice we place a pair of fermionic creation-annihilation operators $c_f, c_f^\dagger$, or, equivalently, a pair of Majorana fermions:

$$\gamma_f \equiv c_f + c_f^\dagger, \qquad \gamma_f' \equiv (c_f - c_f^\dagger)/i. \qquad (7)$$

The even fermionic algebra consists of local observables with a trivial fermion parity, i.e., local observables that commute with the total fermion parity $(-1)^F \equiv \prod_f (-1)^{c_f^\dagger c_f}$. The even algebra is generated by [2]

1. on-site fermion parity

$$P_f \equiv -i\gamma_f \gamma_f'; \qquad (8)$$

2. the Fermionic hopping term

$$S_e \equiv i\gamma_{L(e)}\gamma_{R(e)}', \qquad (9)$$

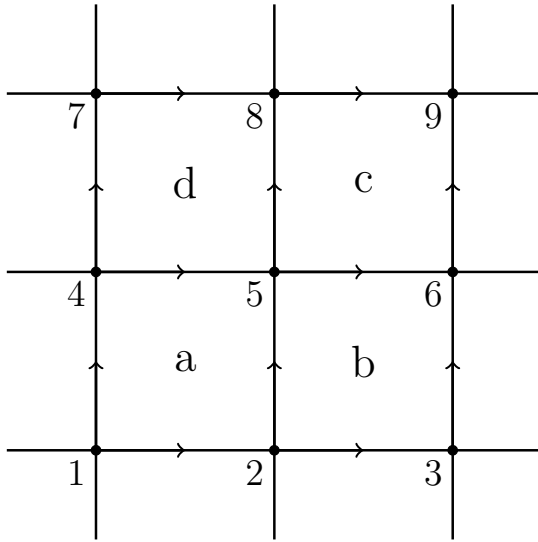where $L(e)$ and $R(e)$ are faces to the left and right of e, with respect to the orientation of e in Fig. 2.

FIG. 2. Bosonization on a square lattice [2]. We put Pauli matrices X_e, Y_e, Z_e on each edge and one complex fermion $c_f, c_f^\dagger$ at each face. In this figure, faces are labeled a–d and vertices are labeled 1–9. Each edge contains a qubit. We work on the Majorana basis $\gamma_f \equiv c_f + c_f^\dagger$ and $\gamma_f' \equiv -i(c_f - c_f^\dagger)$ for convenience.

The bosonic dual of this system involves $\mathbb{Z}_2$-valued spins (qubits) on the edges of the square lattice, generated by the Pauli matrices X_e, Y_e, and Z_e. For every edge e, we define a unitary operator U_e that squares to 1. Here, we label an edge that connects vertices j, k by e_{jk}. For example, in Fig. 2, the edge between faces b and c is labeled as edge e_{56} and the edge between faces c and d is e_{58}. On these edges, we define the corresponding operators,

$$U_{e_{56}} \equiv X_{e_{56}} Z_{e_{25}}, \qquad U_{e_{58}} \equiv X_{e_{58}} Z_{e_{45}}, \qquad (10)$$

where $X_{e_{jk}}$, $Z_{e_{jk}}$ are Pauli matrices acting on a qubit at each edge e_{jk}. Operators U_e for other edges are defined using translational symmetry. Pictorially, the operator $U_{e_{jk}}$ is drawn as

$$U_{e_{jk}} \equiv \quad \begin{array}{c} k \\ | \\ X_{e_{jk}} \\ | \\ -Z- j \end{array} \quad \text{or} \quad \begin{array}{c} j\; -X_{e_{jk}}-\; k \\ | \\ Z \\ | \end{array}, \qquad (11)$$

corresponding to the vertical or horizontal edge e_{jk}. It has been shown in Ref. [2] that U_e and S_e satisfy the same commutation relations. On each face f, we also define the "flux operator" $W_f \equiv \prod_{e \subset f} Z_e$, the product of Z_e around a face f:

$$W_f \equiv \begin{array}{c} -Z- \\ | \quad | \\ Z \quad f \quad Z. \\ | \quad | \\ -Z- \end{array} \qquad (12)$$

The bosonization map, which preserves the commutation relation between operators, is

$$S_e \longleftrightarrow U_e, \qquad P_f \longleftrightarrow W_f, \qquad (13)$$

or, pictorially,

$$i \times \begin{array}{c} \gamma_{L(e)} \\ \underline{\quad e \quad} \\ \gamma'_{R(e)} \end{array} \quad \longleftrightarrow \quad \begin{array}{c} -X_e- \\ Z \\ | \end{array}, \qquad (14)$$

$$i \times \quad \gamma_{L(e)} \begin{array}{|c|} e \;\; \gamma'_{R(e)} \end{array} \quad \longleftrightarrow \quad \begin{array}{c} | \\ X_e \\ -Z- | \end{array}, \qquad (15)$$

$$-i\gamma_f \gamma'_f \quad \longleftrightarrow \quad \begin{array}{c} -Z- \\ | \quad | \\ Z \quad f \quad Z \\ | \quad | \\ -Z- \end{array}. \qquad (16)$$

On the fermionic side, operators S_e and P_f satisfy an additional condition $P_a P_c S_{e_{58}} S_{e_{56}} S_{e_{25}} S_{e_{45}} = 1$ [38]. This generates the gauge constraints (stabilizer) $G_v \equiv W_c \prod_{e \supset v_5} X_e = 1$ imposed by hand on bosonic operators, or, pictorially,

$$G_v \equiv \begin{array}{c} -Z- \\ | \quad | \\ X Z \;\; f \;\; Z \\ | \quad | \\ -X- v -XZ- \\ | \\ X \\ | \end{array} = 1. \qquad (17)$$

The gauge constraint (17) can be considered as the stabilizer ($G_v |\Psi\rangle = |\Psi\rangle$ for $|\Psi\rangle$ in the codespace), which forms the stabilizer group $\mathcal{G}$. The operators U_e and W_f generate all logical operators [39]. In the setting above, qubits live on edges and fermions live on faces, so the ratio between the number of qubits and the number of fermions is $r = 2$. We are going to apply finite-depth GLU transformations to lower this ratio.

B. Compact fermion-to-qubit mapping with ratio $r = 1.5$

In the exact bosonization on the square lattice, the bosonic subspace is constrained by stabilizer (17) at each vertex. First, we enlarge the unit cell to be a 2×2 square, as in Fig. 3. Note that we have colored the faces to be even or odd as the checkerboard. In each 2×2 square, there are in total four fermions, eight qubits, and four stabilizers, whose qubit-fermion ratio is $r = 8/4 = 2$. We apply

even	odd	even	odd
odd	even	odd	even
even	odd	even	odd
odd	even	odd	even

FIG. 3. We color the faces to "even" and "odd." Each edge contains a qubit.

a finite-depth GLU circuit to disentangle some qubits and reduce the ratio.

In Fig. 4, the translation-invariant Clifford circuit is defined. We divide the stabilizers into two cases, living on

an odd face or an even face, as

$$
G_{v,\mathrm{odd}} = \begin{array}{c} -Z- \\ X Z \text{ odd } Z \\ -X- v -XZ- \\ X \end{array}, G_{v,\mathrm{even}} = \begin{array}{c} -Z- \\ X Z \text{ even } Z \\ -X- v -XZ- \\ X \end{array}.
$$

After conjugation by the GLU Clifford circuit V_C defined in Fig. 4, these stabilizers become

$$
V_{\mathrm{C}} \left(\begin{array}{c} -Z- \\ X Z \text{ odd } Z \\ -X- v -XZ- \\ X \end{array} \right) V_{\mathrm{C}}^{\dagger} = \begin{array}{c} \overline{} \\ -Y \text{ odd } \\ v \\ \end{array},
$$

$$(18)$$
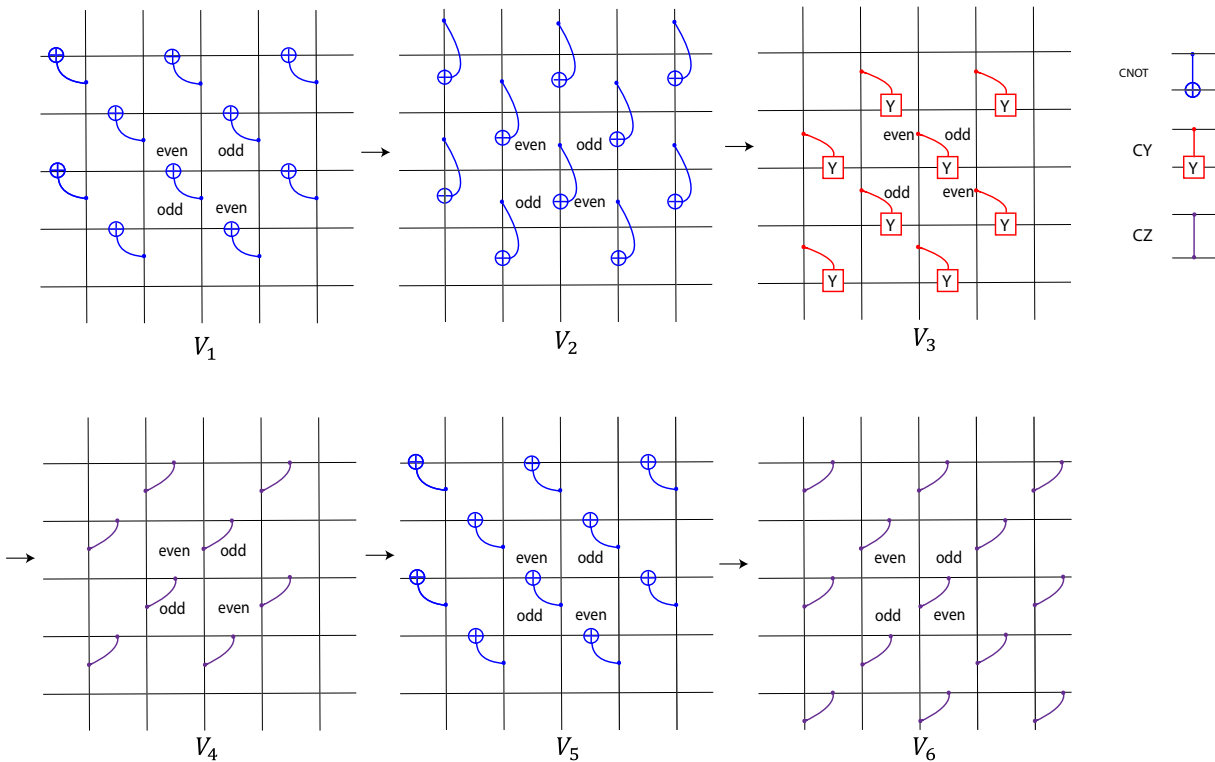
FIG. 4. The finite-depth Clifford circuit for the $r = 1.5$ construction. Here CY denotes the controlled-Y gate. The depicted unitaries are denoted in the sequence as $V_1, V_2, V_3, V_4, V_5, V_6$. The total GLU disentangler is $V_C \equiv V_6 V_5 V_4 V_3 V_2 V_1$. After conjugation by unitary operator V_C, a part of the stabilizers in Eq. (17) becomes a single Pauli matrix, which can be removed from the system.
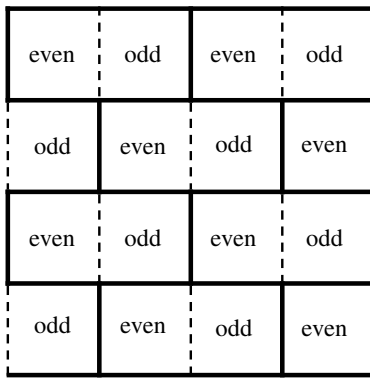
FIG. 5.   The 2d square lattice after disentanglement. The qubits on dashed edges are removed from the system.

$$
V_C \begin{pmatrix} \begin{array}{c} -Z- \\ X\!\!\begin{array}{c}Z\end{array}\text{even} \quad Z \\ -X-\ v\ -XZ- \\ X \end{array} \end{pmatrix} V_C^\dagger = Z \begin{array}{c} X\!\!\begin{array}{c}Z\end{array}\text{even} \\ -X-\ v\ -X- \\ -X-\ -X- \\ X\!\!\begin{array}{c}Z\end{array} \end{array} Z. \tag{19}
$$

We have converted the stabilizer $G_{v,\text{odd}}$ into a single-qubit stabilizer Y up to a sign. This qubit will be in an eigenstate of Y and can be removed. Hence, we successfully eliminated the qubits on the left edges of all odd faces. The qubits only exist on solid edges in Fig. 5, where the dashed lines do not contain any degree of freedom. For a 2×2 unit square, only six qubits remain, and the ratio between qubits and fermions is $6/4 = 1.5$.

By the Clifford circuits in Fig. 4, we eliminate stabilizers on odd faces and convert the stabilizers on even faces to toric-code-like stabilizers. Next, we analyze the logical operators representing fermion hopping after the conjugation. Here the convention of the fermionic hopping is $S_e \equiv i\gamma_{L(e)}\gamma'_{R(e)}$. There are four types of fermionic hopping operators [after removing the degrees of freedom in Eq. (18)]. The first two are horizontal hopping operators,

$$
V_C \begin{pmatrix} \text{odd}\ X_e \\ -Z- \end{pmatrix} V_C^\dagger = \begin{array}{c} -Z- \\ \text{odd}\ X_e \\ -Z- \end{array},
$$

$$
V_C \begin{pmatrix} \text{even}\ X_e \\ -Z- \end{pmatrix} V_C^\dagger = \begin{array}{c} -Z- \\ \text{even}\ e \quad Z \\ -Y-\ -X- \\ Y \end{array}, \tag{20}
$$

and the next two are vertical hopping operators,

$$
V_C \begin{pmatrix} -X_e- \\ Z\ \text{odd} \end{pmatrix} V_C^\dagger = \begin{array}{c} -X_e- \\ \text{odd} \end{array},
$$

$$
V_C \begin{pmatrix} -X_e- \\ Z\ \text{even} \end{pmatrix} V_C^\dagger = \begin{array}{c} -X_e- \\ \text{even} \end{array}, \tag{21}
$$

and two types of flux operators,

$$
V_C \begin{pmatrix} -Z- \\ Z\ \text{odd}\ Z \\ -Z- \end{pmatrix} V_C^\dagger = \begin{array}{c} -Z- \\ \text{odd}\ Z \\ -Z- \end{array},
$$

$$
V_C \begin{pmatrix} -Z- \\ Z\ \text{even}\ Z \\ -Z- \end{pmatrix} V_C^\dagger = \begin{array}{c} -Z- \\ Z\ \text{even} \\ -Z- \end{array}. \tag{22}
$$

We note that the stabilizer in Eq. (19) is the same as the stabilizer of the compact encoding in Ref. [9] (up to relabeling Pauli matrices X, Y, Z). Since the stabilizers are the same, the spaces of logical operators are equivalent. We can redefine the two lines of Eq. (20) as the "on-site fermion parity" and treat Eq. (22) as the "hopping term," which is equivalent to re-pairing the Majorana fermions as in Fig. 6, which reproduces the compact encoding in Ref. [9].

C. Supercompact fermion-to-qubit mapping with ratio $r = 1.25$

In the $r = 1.5$ construction, we label faces with "even" and "odd." Next, we further color the lattice, as in Fig. 7, yellow, blue, red, and green. Yellow and red belong to
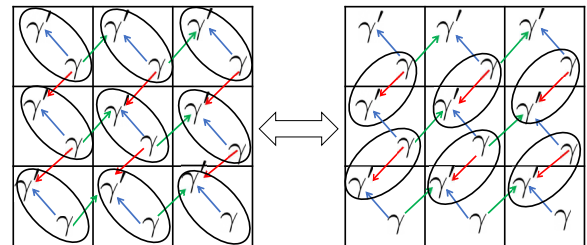

FIG. 6.   The $r = 1.5$ construction is the same as the compact fermion-to-qubit mapping [9] after the re-pairing of Majorana fermions above. Each circle represents a complex fermion formed by the two Majorana fermions. The underlying arrows specify the order to form a fermion. The arrows form a Kasteleyn orientation, ensuring that the fermion parity after re-pairing is well defined [40–42].
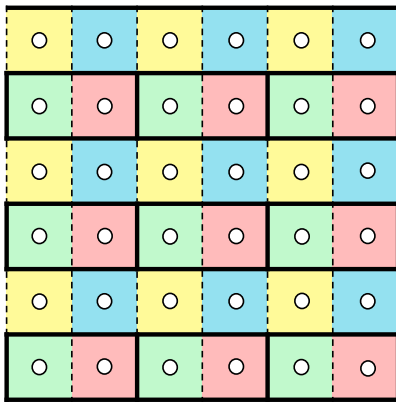
FIG. 7. The 2d square lattice is colored with four colors: yellow, blue, red, and green. Yellow and red belong to the original "odd" faces, and blue and green belong to the original "even" faces. White dots represent fermionic modes inside faces. Compared with Fig. 5, qubits on the edges between yellow and blue faces will be stabilized by a single Pauli matrix after a certain unitary transformation so that they can be removed from the system. In the end, each solid line has one qubit, while there is no qubit on dashed lines.

the "odd" faces, and blue and green belong to the "even" faces. Based on the $r = 1.5$ construction in the previous section, which is obtained from conjugating the original 2d bosonization by the Clifford circuit shown in Fig. 4, we further conjugate the $r = 1.5$ stabilizer (19) by the

Clifford circuit V_{SC} defined in Fig. 8 to generate a new fermion-to-qubit mapping.

Stabilizer (19) (up to a sign) enclosing blue and yellow faces becomes

$$V_{SC} \begin{pmatrix} \text{[grid diagram]} \end{pmatrix} V_{SC}^{\dagger} = \begin{pmatrix} \text{[grid diagram]} \end{pmatrix}. \tag{23}$$

On the other hand, stabilizer (19) (up to a sign) enclosing green and red faces becomes

$$V_{SC} \begin{pmatrix} \text{[grid diagram]} \end{pmatrix} V_{SC}^{\dagger} = \begin{pmatrix} \text{[grid diagram]} \end{pmatrix}, \tag{24}$$

which is a single Pauli Y. The qubit is disentangled from the rest; therefore, we can remove the qubits on the boundaries between yellow and blue faces. The qubit-fermion ratio reduces to $r = 1.25$. Similarly, we conjugate the logical operators (20) and (22) by the Clifford circuit V_{SC} in Fig. 8, and the results of these logical operators are listed in Fig. 9.
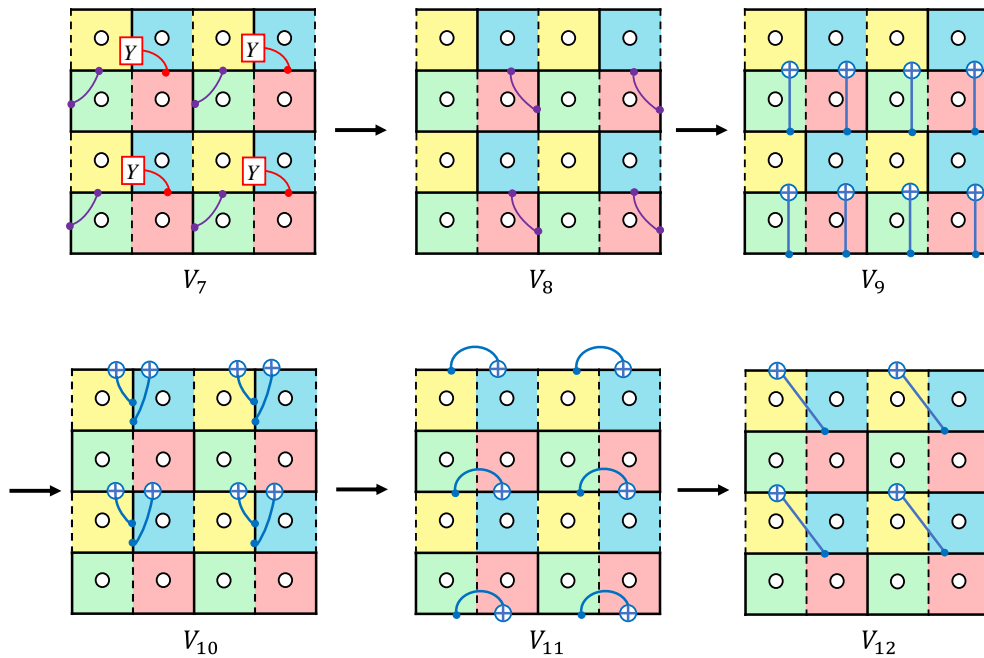

FIG. 8. The finite-depth Clifford circuit to construct bosonization with $r = 1.25$. The depicted unitaries are $V_7, V_8, V_9, V_{10}, V_{11}, V_{12}$ (from top left to bottom right). The GLU disentangler is $V_{SC} = V_{12}V_{11}V_{10}V_9V_8V_7$. After conjugation by the unitary operator V_{SC}, a part of the stabilizers in Eq. (19) becomes a single Pauli matrix, which can be removed from the system.
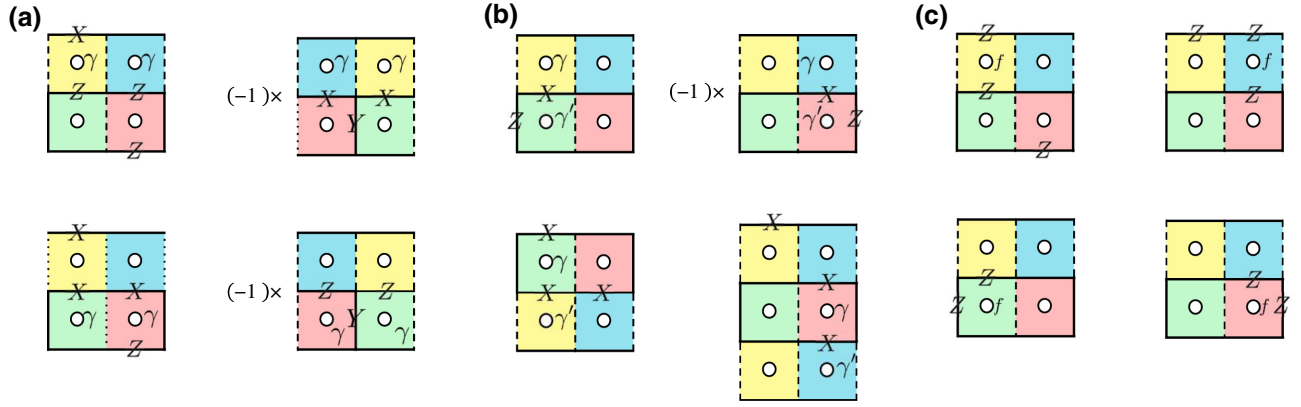
FIG. 9.   Shorthand representation of the mapping between fermionic operators and the Pauli matrices. Panel (a) represents the nearest-neighbor horizontal hopping terms. The first diagram indicates that $i\gamma_{\text{yellow}}\gamma_{\text{blue}}$ is mapped to the Pauli operator $XZZZ$ indicated above. The second diagram (top right) represents that $i\gamma_{\text{blue}}\gamma_{\text{yellow}}$ is mapped to $-XXY$. The remaining diagrams follow the same rule, e.g., $i\gamma_{\text{green}}\gamma_{\text{red}} \leftrightarrow XXXZ$ and $i\gamma_{\text{red}}\gamma_{\text{green}} \leftrightarrow -ZZY$. Panel (b) represents the near-neighbor vertical hopping terms. Note that the fermionic hopping term is γ to γ' in this case. For example, the first diagram is $i\gamma_{\text{yellow}}\gamma'_{\text{green}} \leftrightarrow XZ$. Panel (c) represents the fermion parity operators. Each face f indicates the location of the on-site fermionic parity operator $-i\gamma_f \gamma'_f$, which is mapped to the Pauli ZZZ shown in the diagram.

In Appendix C, we deform the lattice and re-pair the Majorana fermions to obtain a more symmetric representation of this supercompact fermion-to-qubit mapping.

D. General construction for compact fermion-to-qubit mappings

In this section, we describe a general method to construct fermion-to-qubit mappings with a reduced qubit-fermion ratio from the exact bosonization. The exact bosonization contains gauge constraints (stabilizers) (17) supported on faces f (northeast to vertices v), and we rename G_v as G_f for convenience. We enlarge the unit cell and show that it is always possible to apply finite-depth GLU operators such that a portion of the stabilizers can be mapped to a single Pauli matrix. More precisely, we are going to prove that the stabilizer on each white face below can be mapped to a single Pauli matrix, i.e.,


$$(25)$$
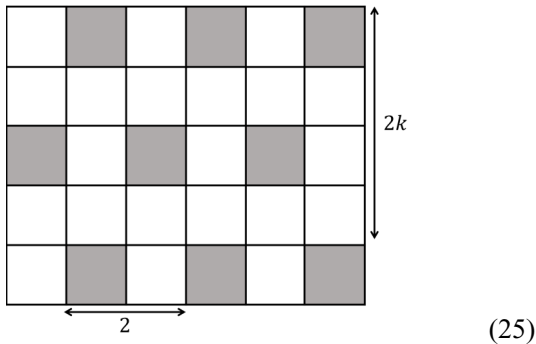
with k any positive integer [43].

Instead of transforming G_f on white faces directly, we are going to prove a stronger statement: the gauge constraints G_f [Eq. (17)] on white faces, the hopping operators U_e [Eq. (51)] across horizontal edges, and the operators

$$G'_f \equiv \left| \begin{array}{c} \overline{\quad -Y- \quad} \\ f \quad X \quad \Big| \quad Z, \\ \underline{\hspace{2em}} \end{array} \right.$$

$$(26)$$

on gray faces can all be mapped to a single Pauli matrix simultaneously under a finite-depth GLU circuit. These operators on the square lattice are as follows:

$$(27)$$
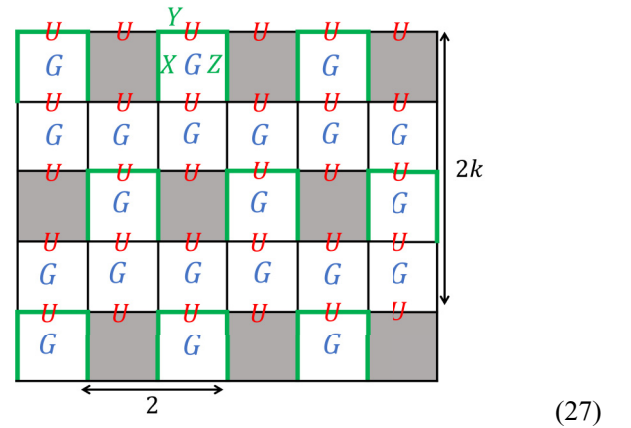
To prove the above statement, we need to introduce a lemma.

Lemma 1: *Given $\tilde{Z}_e$ and $\tilde{X}_e$ for all edges that are products of Pauli matrices on a neighborhood of the edge e satisfying the Pauli algebra,*

$$[\tilde{X}_e, \tilde{X}_{e'}] = [\tilde{Z}_e, \tilde{Z}_{e'}] = 0, \qquad \tilde{X}_e \tilde{Z}_{e'} = (-1)^{\delta_{e,e'}} \tilde{Z}_{e'} \tilde{X}_e,$$

there exists a finite-depth GLU transformation mapping $\tilde{X}_e, \tilde{Z}_e$ to X_e, Z_e (a single Pauli on edge e).

Proof. The (Clifford) QCA in two spatial dimensions are simply (Clifford) local unitary circuits and shifts [34,35]. The map

$$\alpha(X_e) = \tilde{X}_e, \qquad \alpha(Z_e) = \tilde{Z}_e, \qquad (28)$$

defines a QCA and can be decomposed into a Clifford circuit and shifts. For the shift operator, we can introduce ancilla in the $|0\rangle$ states and define the shift operator moving the ancilla in the opposite direction, such that the net flow of qubits is zero. Then, this shift operator can be expressed by a local unitary circuit (involving the ancilla degrees of freedom). Ultimately, these ancilla qubits are still in the $|0\rangle$ states and can be removed by a finite-depth GLU transformation. Therefore, there exists a finite-depth GLU transformation from X_e, Z_e to $\tilde{X}_e, \tilde{Z}_e$, and vice versa. ∎

Lemma 2: *Given operators $\tilde{Z}_e$ (separators) and $\overline{X}_e$ (flippers) that are products of Pauli matrices on a neighborhood of the edge e satisfying*

$$[\tilde{Z}_e, \tilde{Z}_{e'}] = 0, \qquad \overline{X}_e \tilde{Z}_{e'} = (-1)^{\delta_{e,e'}} \tilde{Z}_{e'} \overline{X}_e, \qquad (29)$$

there exist operators $\tilde{X}_e$ that are products of Pauli matrices on a neighborhood of edges e such that

$$[\tilde{X}_e, \tilde{X}_{e'}] = [\tilde{Z}_e, \tilde{Z}_{e'}] = 0, \qquad \tilde{X}_e \tilde{Z}_{e'} = (-1)^{\delta_{e,e'}} \tilde{Z}_{e'} \tilde{X}_e.$$

In other words, if the flippers do not commute with themselves, they can be modified such that the Pauli algebra is satisfied.

Proof. If $\overline{X}_e$ and $\overline{X}_{e'}$ do not commute,

$$\overline{X}_e \overline{X}_{e'} = -\overline{X}_{e'} \overline{X}_e, \qquad (30)$$

we define

$$\tilde{X}_e \equiv \overline{X}_e \tilde{Z}_{e'}, \qquad \tilde{X}_{e'} \equiv \overline{X}_{e'}. \qquad (31)$$

Note that $\tilde{Z}_{e'}$ only affects the commutation relation between e and e' and this fixes the commutation for the X part and leaves the Z part unchanged. Therefore, $\tilde{X}_e$ and $\tilde{Z}_e$ satisfy the Pauli algebra. ∎

The operators $\tilde{Z}_e$ and $\overline{X}_e$ are called separators and flippers [44]. Once the separators and flippers are given, a QCA is defined by Eq. (28) [after defining $\tilde{X}_e$ by Eq. (31)]. By Lemma 1, the separator can be mapped to a single Pauli matrix by a finite-depth GLU transformation.

The operators G_f on white faces, U_e on horizontal edges, and G'_f on gray faces in schematic (27) are the separators $\tilde{Z}_e$. We now describe their flippers.

1. For G'_a on a gray face a, we define its flipper by the product of X_e (m strings of the toric code) connecting two gray faces on the column to the right, as shown in Fig. 10. It can be checked that this m string only violates exactly one G'_f and commutes with all other separators G_f and U_e.

2. A "potential" flipper [45] for the separator G_b on a white face b is the product of X connecting the white face to the gray face below (Fig. 10). This operator flips exactly one of the G_f on a white face and commutes with all U_e, but it may fail to commute with a G'_f on a gray face. In this case, we can always attach the flipper for this G'_f (found in step 1) to the potential flipper. This operator becomes the true flipper for a single G_f.

3. For U_1 on a horizontal edge 1, we start with a potential flipper Z on this edge 1. It is obvious that it flips only one U_e and fails to commute a finite number of G_f and G'_f on white and gray faces. Since we have already found the flippers for G_f and G'_f, we can attach these flippers to the potential flipper such that the combined operator commutes will all separators except this U_1.

We have found the complete set of separators and flippers on the square lattice. By Lemma 1, the G_f on each white face can be mapped to a single Pauli matrix.
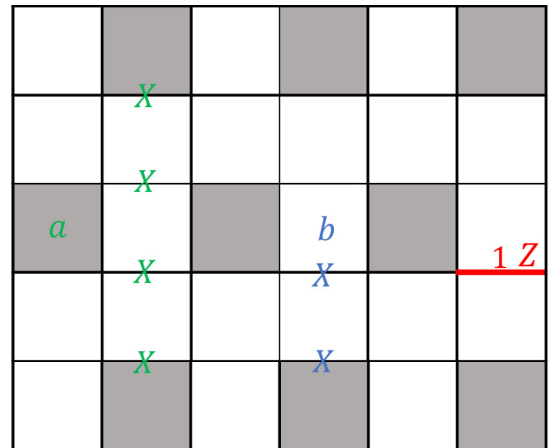

FIG. 10. The (potential) flippers. For G'_a on the gray face a, its flipper is the product of X connecting two gray faces on its right column, shown by the green operator. For G_b on the white face, its potential flipper is the product of X connecting to a gray face below, shown by the blue operator. This potential flipper may anticommute with G' on a gray face, which can be fixed by attaching the flipper for this G'. For U_{e_1} on a horizontal edge e_1, the potential flipper is Z_{e_1}, which flips exactly one U_e and anticommutes with some G_f and G'_f on white and gray faces. This can be fixed by attaching the flippers for these G_f and G'_f to the potential flipper of U_{e_1}.

III. EQUIVALENCE BETWEEN FERMION-TO-QUBIT MAPPINGS AND THE EXACT BOSONIZATION

In this section, we argue that any locality-preserving fermion-to-qubit mappings [46] in two spatial dimensions can be connected to the exact bosonization by a finite-depth GLU transformation. First, given a fermion-to-qubit mapping, it must contain the flux operators $\tilde{W}$ (images of the local fermion parity) and the gauge constraints $\tilde{G}$ (images of the product of fermionic hopping terms in a small closed loop). On a torus, we can define a Pauli stabilizer code as

$$H = -\sum \tilde{G} - \sum \tilde{W}. \tag{32}$$

Over two large cycles of the torus, we have the four-fold ground-state degeneracy since we do not impose the fermionic constraints on the large cycles. The code distance is linear in the system size since the logical operator is the product of hopping along with the large cycles. It is proven in Ref. [47] that any translationally invariant $\mathbb{Z}_p$ Pauli stabilizer model with a linear code distance is decomposed by a local Clifford circuit of constant depth into a finite number of copies of the toric code for any prime p [48]. Since the degeneracy is four on the torus, the stabilizer code in Eq. (32) must be a single copy of the toric code up to a Clifford circuit. Therefore, $\tilde{G}$ and $\tilde{W}$ are related to G_v and W_f in the exact bosonization in Sec. II A by a GLU transformation (since the toric codes defined on different lattices are related by a GLU transformation to add or remove qubits).

Note that the above discussion works for arbitrary lattices with a spinless fermionic mode on each face. Moreover, we can divide the faces into different sets, i.e., black and white faces on the checkboard, and associate the spin or other degrees of freedom with each set [49]. Those labels do not affect the above argument based on Ref. [47]. Therefore, the equivalence between fermion-to-qubit mappings is also true for spinful fermions.

In the following part of this section, we explicitly demonstrate how to transform many well-known fermion-to-qubit mappings in the literature to the exact bosonization by finite-depth GLU Clifford circuits. For each example, we first demonstrate their logical operators and stabilizers. Next, we construct finite-depth Clifford circuits that transform the logical operators and stabilizers of different fermion-to-qubit mappings to those in the 2d exact bosonization.

A. Bravyi-Kitaev superfast simulation

The BKSF encoding in Ref. [11] is a method to encode fermionic operators into Pauli operators. BKSF encoding encodes complex fermions at vertices v by qubits on edges e. The key idea of BKSF encoding is to assign an arbitrary ordering of edges around each vertex and define the logical operators according to the ordering. The fermions are put at the graph's vertices, represented by Majorana operators γ_v, γ'_v for each vertex v. The even algebra of fermions is generated by

$$A_{e_{jk}} = i\gamma_j \gamma_k, \qquad B_v = -i\gamma_v \gamma'_v, \tag{33}$$

where $A_{e_{jk}}$ is defined on each edge e_{jk}, the edge between vertices j and k, and B_v is defined at each vertex v. Note that $A_{e_{jk}}$ and B_v anticommute if and only if vertex v coincides with either vertex j or k, and A_e and $A_{e'}$ anticommute if and only if e and e' are two different edges connecting to the same vertex. We construct Pauli operators living on edges to capture the same algebra as A_e and B_v.

For vertex v, we label the edges connected to v with numbers $1, 2, 3, 4$ on the square lattice, shown in Fig. 11. Therefore, for two edges e, e' connecting to the same vertex, the ordering between them is defined by the assigned number, i.e., either $e < e'$ or $e > e'$. Now, we can define the logical operator

$$\tilde{A}^{\text{BK}}_{e_{jk}} = X_e \prod_{e' \supset j \,|\, e' < e} Z_{e'} \prod_{e'' \supset k \,|\, e'' < e} Z_{e''}, \tag{34}$$

where $e' \supset j$ and $e'' \supset k$ mean that all edges e' connect to vertex j and all edges e'' connect to vertex k, and the other logical operator

$$\tilde{B}^{\text{BK}}_v = \prod_{e \supset v} Z_e, \tag{35}$$

which is the product of the Pauli Z_e on all edges connected to vertex v. From the Pauli Z in Eq. (34), $\tilde{A}^{\text{BK}}_e$ and $\tilde{A}^{\text{BK}}_{e'}$
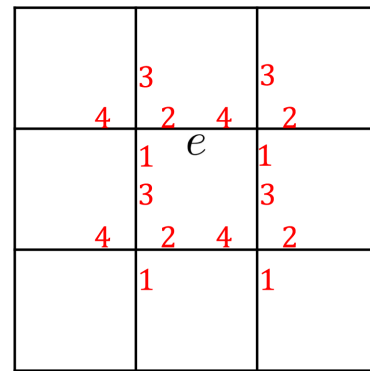

FIG. 11. The ordering of edges on each vertex. The red numbers are the labels. Note that one edge is connected to two vertices, and the two numbers on the two vertices do not need to be the same. The assigned numbers determine the relative ordering for two edges connecting to the same vertex.

anticommute if and only if e and e' are connecting to the same vertex v since we have either

$$\tilde{A}_e^{\mathrm{BK}} = X_e \cdots \quad \text{and} \quad \tilde{A}_{e'}^{\mathrm{BK}} = X_{e'} Z_e \cdots \quad \text{for } e < e' \quad (36)$$

or

$$\tilde{A}_e^{\mathrm{BK}} = X_e Z_{e'} \cdots \quad \text{and} \quad \tilde{A}_{e'}^{\mathrm{BK}} = X_{e'} \cdots \quad \text{for } e > e', \quad (37)$$

where "$\cdots$" denotes the Pauli matrices on other edges irrelevant to the commutation relation. Operators $\tilde{A}_e^{\mathrm{BK}}$ and $\tilde{B}_v^{\mathrm{BK}}$ are designed to have the same commutation relations as A_e and B_v in Eq. (33).

The fermion-to-qubit mapping is

$$A_{e_{jk}} \longleftrightarrow \tilde{A}_{e_{jk}}^{\mathrm{BK}}, \qquad B_v \longleftrightarrow \tilde{B}_v^{\mathrm{BK}}. \quad (38)$$

For each closed loop l in the graph, the product of $\tilde{A}_e^{\mathrm{BK}}$ on this loop needs to satisfy the condition

$$\prod_{e \in l} \tilde{A}_e^{\mathrm{BK}} = i^{|l|}, \quad (39)$$

where $|l|$ is the length of loop l. This is due to the identity of Majorana operators. For example, substituting A_e into Eq. (33), we have the identity $A_{e_{12}} A_{e_{23}} A_{e_{31}} = (i\gamma_{v_1}\gamma_{v_2})(i\gamma_{v_2}\gamma_{v_3})(i\gamma_{v_3}\gamma_{v_1}) = i^3$.

By the convention in Fig. 11, we have

$$i\gamma_j\gamma_k' \longleftrightarrow i\tilde{A}_{e_{jk}}^{\mathrm{BK}}\tilde{B}_k^{\mathrm{BK}} = \begin{array}{cc} \begin{matrix} j \\ | \\ Y_{e_{jk}} \\ | \\ \!-\!\!Z\!\!-\! k \end{matrix} & \begin{matrix} j -Y_{e_{jk}}- k \\ Z \\ | \end{matrix} \end{array}. \quad (40)$$

We note that this is the same logical operator as the exact bosonization in the dual lattice after we relabel the Pauli matrices X and Y. The fermion parity terms in both cases are a product of Z around a vertex (a face in the dual lattice). Therefore, the BKSF approach with this ordering convention is the same as the exact bosonization.

Note that, from the construction of the logical operator $\tilde{A}_{e_{jk}}^{\mathrm{BK}}$ in Eq. (34), the only property we used from the assigned numbers is that they determine the ordering of two edges at the same vertex. If fact, if all "relative orderings" [50] for a pair of edges connecting to the same vertex are defined, the construction in Eq. (34) is still valid. Given a construction from a choice of relative orderings, if we want to redefine the relative ordering between a pair of edges e and e', i.e., swapping between two cases in Eqs. (36) and (37), we can simply conjugate the $\mathrm{CZ}_{e,e'}$ gate on the system. Therefore, the BKSF approach with different choices of relative orderings can be transformed from one to another by conjugating a product of controlled-Z (CZ) gates. This agrees with the main result: all fermion-to-qubit mappings are related by GLU operators.

B. Verstraete-Cirac auxiliary method

In this section, we demonstrate the equivalent relation between the Verstraete-Cirac mapping [3] and exact bosonization after regrouping Majorana fermions. The basic idea of the Verstraete-Cirac mapping is to eliminate the nonlocal Pauli-Z string from the 1d Jordan-Wigner transformation by introducing auxiliary qubits with gauge constraints. In this mapping, each site i uses four Majorana modes $\gamma_i, \gamma_i', \tilde{\gamma}_i, \tilde{\gamma}_i'$ to encode a complex fermion and an auxiliary complex fermion. For implementation, we put two qubits on each vertex, one for the physical complex fermion and the other for the auxiliary complex fermion. The Majorana operators $\tilde{\gamma}_i, \tilde{\gamma}_i'$ belong to the auxiliary complex fermion. The auxiliary fermions stay in the ground state of the Hamiltonian

$$H_{\mathrm{aux}} = -\sum_{\{j,k\}} P_{jk} = -i \sum_{\{j,k\}} \tilde{\gamma}_j \tilde{\gamma}_k', \quad (41)$$

where $\{j,k\}$ includes only pairs (j,k) that are connected by directed edges in Fig. 12, e.g., $(1,5),(2,6),(5,9),\ldots$. The vertical hopping operator is modified as $c_i^\dagger c_j \to c_i^\dagger c_j (i\tilde{\gamma}_i\tilde{\gamma}_j')$, which does not affect the properties of original fermions in the space of $i\tilde{\gamma}_i\tilde{\gamma}_j' = 1$. We order the first row (odd row) from left to right, the second (even raw) from left to right, and so on, shown as Fig. 12. Next, we apply the 1d Jordan-Wigner transformation with respect to the ordering $1 \to \tilde{1} \to 2 \to \tilde{2} \to 3 \to \tilde{3} \to 4 \to \tilde{4} \to 5 \to \tilde{5} \to 6 \to \tilde{6} \to \cdots$, where j and $\tilde{j}$ represent the physical fermion and auxiliary fermion at site j. The motivation of introducing $i\tilde{\gamma}_i\tilde{\gamma}_j'$ is to cancel the nonlocal Z string for the $c_i^\dagger c_j$ term after the Jordan-Wigner transformation. If
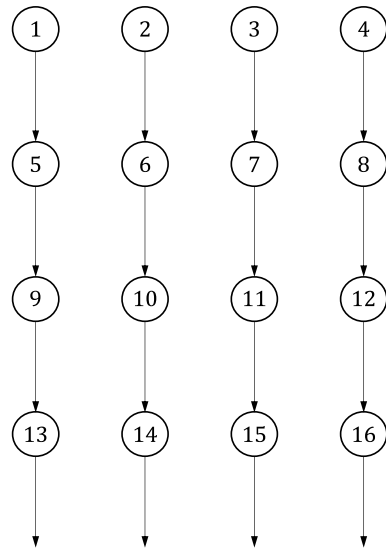

FIG. 12. Graph structure of the auxiliary Hamiltonian H_{aux}.

the auxiliary system is in the $+1$ eigenspace of $i\widetilde{\gamma}_i\widetilde{\gamma}'_j$., this extra term would not affect the property of the system.

However, the auxiliary Hamiltonian becomes a nonlocal Hamiltonian after the Jordan-Wigner transformation. To resolve this problem, we perform the substitution $P_{15} \rightarrow P_{15}P_{26}$, $P_{26} \rightarrow P_{26}P_{37}$, etc. Since all P commute with each other and are in $+1$ eigenstates, this substitution does not change the ground-state space [51]. Then the constraint $P_{ik}P_{jl} = -\widetilde{\gamma}_i\widetilde{\gamma}'_k\widetilde{\gamma}_j\widetilde{\gamma}'_l = 1$ is mapped to a local gauge constraint (stabilizer) after the Jordan-Wigner transformation:

$$P_{ik}P_{jl} \rightarrow G_v^{\mathrm{VC}} \equiv \begin{array}{c} I_i \qquad Z_j \\ \mid \qquad \mid \\ -\widetilde{X}_i - v - \widetilde{Y}_j - \\ I_k \qquad Z_l \\ \mid \qquad \mid \\ -\widetilde{Y}_k - \quad -\widetilde{X}_l - \end{array} , \tag{42}$$

Here the Pauli matrices $\{\widetilde{X}_n, \widetilde{Y}_n, \widetilde{Z}_n\}$ act on the auxiliary qubit n. We put physical qubits on vertical edges and auxiliary qubits on horizontal ones. Since physical qubits and auxiliary qubits are on different edges, we will not show the tilde in the following text for convenience. The hopping operators [S_e in Eq. (9)] and fermion parity operators [P_f in Eq. (8)] are mapped to

$$U_e^{\mathrm{VC}} \equiv \begin{array}{c} X \\ \mid \\ -Y_e - \\ Y \\ \mid \\ -X - \end{array} , \qquad \begin{array}{c} X \qquad X_e \\ \mid \qquad \mid \\ \quad -Z- \end{array}$$

$$W_f^{\mathrm{VC}} \equiv \boxed{\overline{\,Z \quad f\,}} \,. \tag{43}$$

By conjugating stabilizer (42) by the Clifford circuits V^{VC} shown in Fig. 13, the new stabilizer is

$$V^{\mathrm{VC}} G_v^{\mathrm{VC}} (V^{\mathrm{VC}})^\dagger = \begin{array}{c} -Z- \\ \mid XZ \qquad \mid Z \\ -X- v -XZ- \\ \mid \\ X \end{array} , \tag{44}$$

which is precisely the gauge constraint (17) of the exact bosonization. This implies that the logical space should also be the same as the exact bosonization. Conjugating the logical operators (43) by V^{VC}, we obtain the new logical
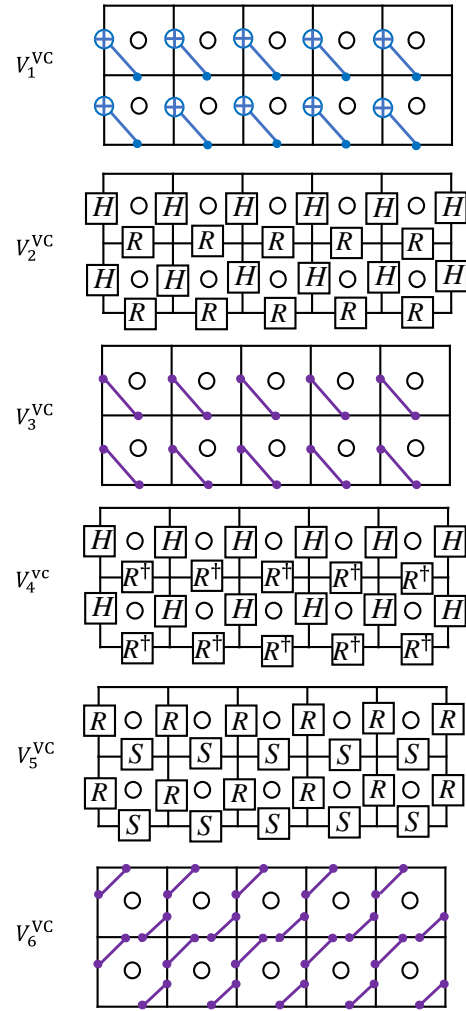

FIG. 13. The finite-depth Clifford circuit to convert the Verstraete-Cirac mapping to the exact bosonization. Details of the H, R, S gates are discussed in Appendix B. The finite-depth Clifford circuit that converts the Verstraete-Cirac mapping into the exact bosonization is $V^{\mathrm{VC}} = V_6^{\mathrm{VC}} V_5^{\mathrm{VC}} V_4^{\mathrm{VC}} V_3^{\mathrm{VC}} V_2^{\mathrm{VC}} V_1^{\mathrm{VC}}$.

operators

$$V^{\mathrm{VC}} U_e^{\mathrm{VC}} (V^{\mathrm{VC}})^\dagger = \begin{array}{c} -e- \\ \mid \\ X \\ \mid \\ -Z- \end{array} , \quad \begin{array}{c} e \\ \mid \\ -X- \mid \\ Z \\ \mid \end{array} , \tag{45}$$

and

$$V^{\mathrm{VC}} W_f^{\mathrm{VC}} (V^{\mathrm{VC}})^\dagger = \begin{array}{c} \boxed{\overline{\quad f \quad}} \\ -Y- \\ Y \\ \mid \end{array} . \tag{46}$$
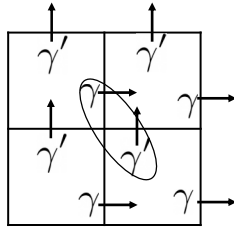
FIG. 14. To match our exact bosonization to the Verstraete-Cirac mapping, we shift our Majorana modes on each face in the following way: (1) shift γ_f' upward and let it be γ on the new face; (2) shift γ_f rightward and let it be γ' on the new face.

If we shift the Majorana fermions in the exact bosonization as in Fig. 14 and re-pair them, then we find that the exact bosonization and the Verstraete-Cirac mapping are equivalent; see Fig. 15. The new logical operators and stabilizers are precisely the logical operators and stabilizers of exact bosonization after this shift.

C. Kitaev's honeycomb model

The Hamiltonian of Kitaev's honeycomb model [4] can be written as

$$H = -J_x \sum_{x-\text{links}} X_j^A X_k^B - J_y \sum_{y-\text{links}} Y_j^A Y_j^B$$
$$- J_z \sum_{z-\text{links}} Z_j^A Z_k^B, \qquad (47)$$

where the x, y, z links are shown in Fig. 16. The qubit at each site j can be represented by four Majorana operators, b_j^x, b_j^y, b_j^z, and γ_j, with an additional constraint

$$D_j = b_j^x b_j^y b_j^z \gamma_j = 1$$
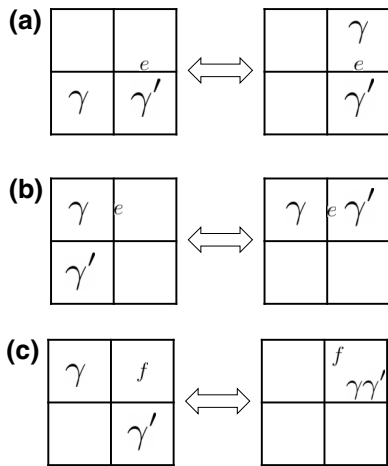
FIG. 15. Correspondence of logical operators between the exact bosonization and the Verstraete-Cirac mapping.
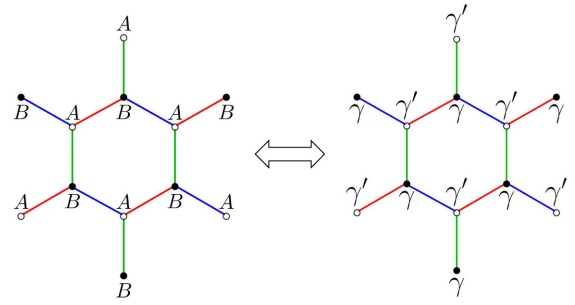
FIG. 16. Kitaev's honeycomb model. The red, blue, and green edges represent x, y, and z links. For each link, the product of two Pauli matrices on its vertices is mapped to the product of γ and γ' on its vertices, shown in Eq. (50).

to eliminate the redundancy at each site j. The Pauli matrices at each site j are represented as

$$X_j = ib_j^x \gamma_j, \qquad Y_j = ib_j^y \gamma_j, \qquad Z_j = ib_j^z \gamma_j. \qquad (48)$$

Then, a free-fermion Hamiltonian

$$H = \frac{i}{2} \sum_{e_{jk}} J_{\alpha jk} \gamma_j^A \gamma_k^B \qquad (49)$$

is equivalent to a sector of Eq. (47), where the index α takes values x, y, or z depending on the direction of link jk. Focusing on the algebra generated by γ_j in a fixed sector, mapping (48) induces a correspondence [2,4]:

$$i\gamma_j^A \gamma_k^B \longleftrightarrow \begin{cases} X_j^A X_k^B & \text{if } jk \in x \text{ link,} \\ Y_j^A Y_k^B & \text{if } jk \in y \text{ link,} \\ Z_j^A Z_k^B & \text{if } jk \in z \text{ link.} \end{cases} \qquad (50)$$

Since the product of Majorana hoppings along a hexagon is proportional to identity, which gives a gauge constraint on the qubit Hilbert space, we can show that the exact bosonization [2] can be obtained by embedding the honeycomb lattice into the square lattice. The details of such a procedure are as follows. Starting from the 2d exact bosonization, we shift and relabel the Majorana fermions as in Fig. 17. After this relabeling and shift of the Majorana fermion, we conjugate every qubit by a Hadamard gate that implements the transformation $HXH^\dagger = Z, HZH^\dagger = X$. The complete bosonization map becomes

$$i \times \underset{\gamma_{R(e)}'}{\overset{\gamma_{L(e)}}{\underline{\qquad e \qquad}}} \longleftrightarrow \underset{-X_e-}{\overset{Z,}{\big|}} \qquad (51)$$
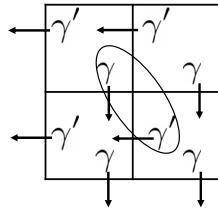
FIG. 17. To match our exact bosonization to Kitaev's honeycomb model, we shift our Majorana modes on each face in the following way: (1) shift γ_f downward and let it be γ on the new face; (2) shift γ_f' leftward and let it be γ' on the new face. We re-pair γ and γ' enveloped in the ellipse to form a complex fermion.

$$i \times \quad \begin{array}{c|c} \gamma_{L(e)} & e \ \gamma_{R(e)}' \end{array} \quad \longleftrightarrow \quad \begin{array}{c} -Z- \\ X_e \\ | \end{array} \quad , \tag{52}$$

$$-i\gamma_f\gamma_f' \quad \longleftrightarrow \quad \begin{array}{c} -Y- \\ f \ Y \\ | \end{array} \quad , \tag{53}$$

with the stabilizer (gauge constraint)

$$G_v = \begin{array}{c} -X- \\ Z\!X \quad\quad X \\ -Z-\ v\ -ZX- \\ Z \\ | \end{array} = 1. \tag{54}$$

Equations (51)–(53) will correspond to the green, red, and blue links embedded in Fig. 18, respectively. The right-hand sides of these equations are all weight-2 Pauli operators that are similar to the spin-spin interactions in Kitaev's honeycomb model. These operators only differ from Kitaev's honeycomb model by Hadamard gates.
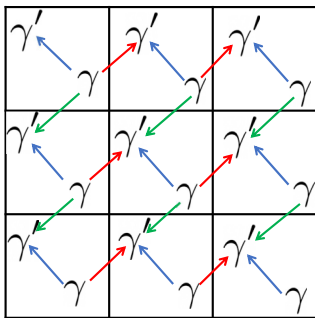
FIG. 18. The embedding of the honeycomb lattice into the square lattice. The red, blue, and green links correspond to the x, y, and z types in Kitaev's honeycomb model.

Once we conjugate all the qubits on horizontal edges by Hadamard gates that switch $X \leftrightarrow Z$, then the right-hand sides of Eqs. (51) and (52) become ZZ and XX interactions as the Z and X edges in Kitaev's honeycomb model while the right-hand side of Eq. (53) still forms a YY term in Kitaev's honeycomb model. Then, we end up with Kitaev's honeycomb model.

D. Majorana loop stabilizer codes

In this section, we show that the MLSC [7] is GLU equivalent to the 2d exact bosonization. Similar to BKSF encoding, Majorana loop stabilizer codes encode a complex fermion on vertex v by qubits on edge e connected to v. Majorana loop stabilizer codes have fermionic hopping
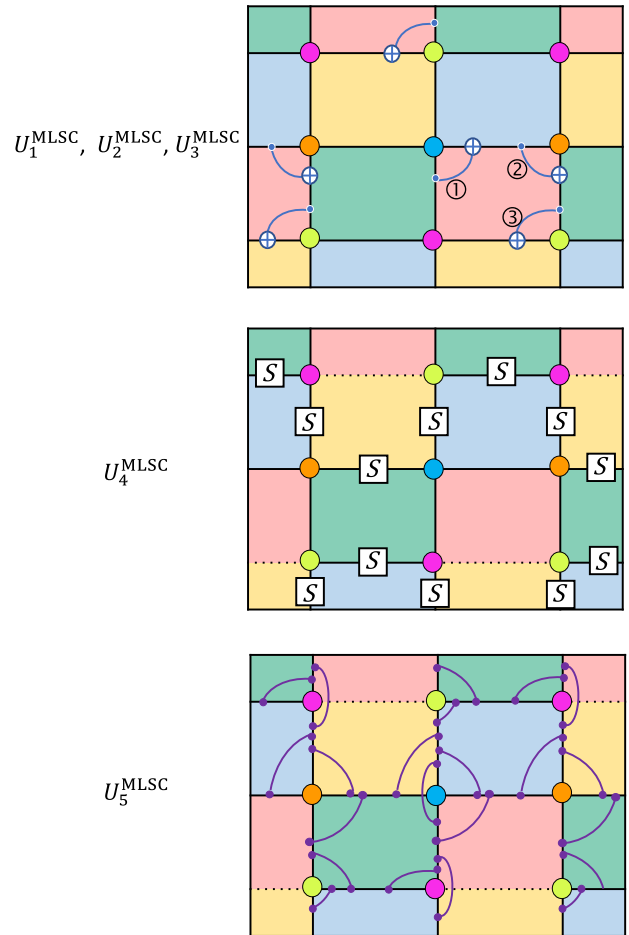

FIG. 19. The finite-depth Clifford circuit for the MLSC to the exact bosonization. The first Clifford circuit will disentangle the qubits on the edges between red and yellow faces, so the edges between red and yellow faces become dashed lines in the second and third steps. The first panel involves three unitary circuits $U_1^{\text{MLSC}}, U_2^{\text{MLSC}}, U_3^{\text{MLSC}}$ corresponding to the controlled-NOT (CNOT) gates labeled ①, ②, and ③, respectively. The finite-depth Clifford circuit that converts Majorana-loop stabilizer codes to the exact bosonization is $U^{\text{MLSC}} = U_5^{\text{MLSC}} U_4^{\text{MLSC}} U_3^{\text{MLSC}} U_2^{\text{MLSC}} U_1^{\text{MLSC}}$.
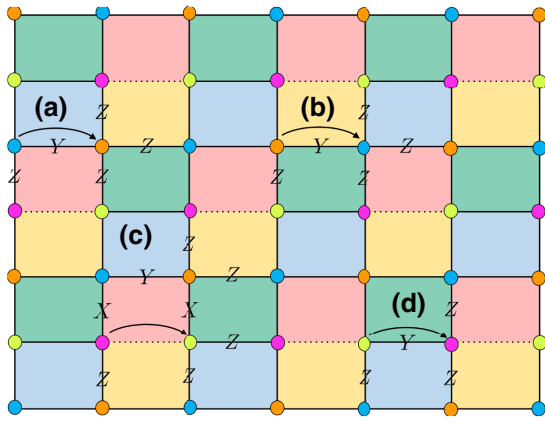
FIG. 20. Horizontal hoppings $i\gamma_{L(e)}\gamma_{R(e)}$ after a finite-depth GLU transformation in Fig. 19. Labels (a) and (b) denote hoppings between blue and orange dots; labels (c) and (d) denote hoppings between pink and yellow dots. Hoppings (a), (b), and (d) are exactly the horizontal hoppings in the exact bosonization, and hopping (c) is a product of the hopping operator and the stabilizer in the exact bosonization.

operation $A_e = i\gamma_{L(e)}\gamma_{R(e)}$ on each edge, fermion parity operator $P_f = -i\gamma_f \gamma_f'$ on each vertex, and stabilizers G_v acting on faces with different colors. We follow the same procedure described in Sec. II, conjugating the logical operations and stabilizers of the MLSC by the finite-depth Clifford circuits in Fig. 19. Then the four kinds of horizontal hoppings in the MLSC reduce to the horizontal hopping in the exact bosonization (up to a stabilizer), and the same thing happens to the vertical hoppings, parity operators, and stabilizers.

Starting from the MLSC, Figs. 20 and 21 show that the horizontal and vertical hoppings $i\gamma_{L(e)}\gamma_{R(e)}$ after the transformation can match the horizontal and vertical hoppings in exact bosonization. An interesting fact is that the first Clifford circuit in Fig. 19 removes qubits on
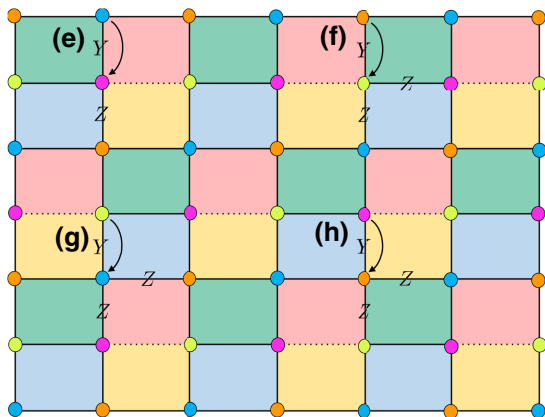
FIG. 21. Labels (e)–(h) denote vertical hoppings $i\gamma_{L(e)}\gamma_{R(e)}$ after a finite-depth GLU transformation in Fig. 19. They match the vertical hoppings in the exact bosonization.

the edges between red and yellow faces and makes this correspondence possible.

E. Connection to the Jordan-Wigner transformation

In this section, we show that conjugating the exact bosonization by a linear-depth [52] Clifford circuit in Fig. 22 will result in the 1d Jordan-Wigner transformation along the path in Fig. 23, where the fermionic hopping $i\gamma_j \gamma_k'$ with j, k in different rows is mapped to a nonlocal Pauli string.

For the Jordan-Wigner transformation, the qubit-fermion ratio is 1, but it is a nonlocal mapping since the vertical hopping terms are mediated by a Pauli-Z string between two sites. By directly applying the linear-depth GLU Clifford circuit in Fig. 22 to the logical operators of the exact bosonization, the qubits on the horizontal edges are disentangled and do not show up in the logical operators. All stabilizers become single-Pauli operators
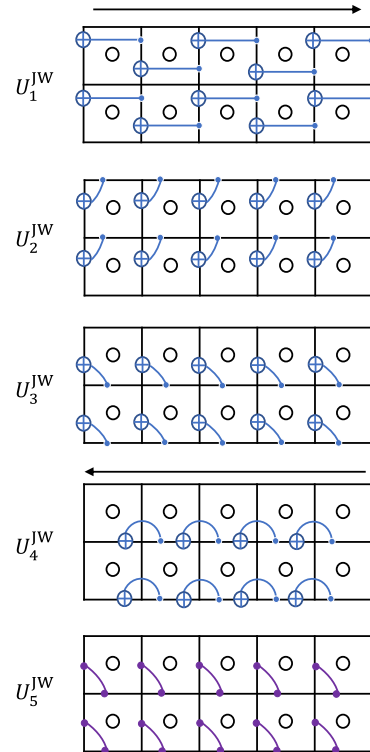

FIG. 22. The finite-depth Clifford circuit to convert the exact bosonization to the 1d Jordan-Wigner transformation. In the first step, we order the system from left to right, then apply the CNOT gate to each column following the above ordering. The CNOT gates are applied simultaneously in the second and third steps. In the fourth step, we order the system from right to left, then apply the CNOT gate to each column following the right-to-left ordering. In the fifth step, CZ gates are simultaneously applied. The depicted unitaries are $U_1^{JW}, U_2^{JW}, U_3^{JW}, U_4^{JW}, U_5^{JW}$ (from top to bottom). The GLU disentangler is $U_{JW} = U_5^{JW} U_4^{JW} U_3^{JW} U_2^{JW} U_1^{JW}$. Note that U_1^{JW} and U_4^{JW} are linear-depth local unitary circuits.

on horizontal edges and can be removed by GLU transformations. Explicitly, the horizontal and vertical hoppings are

$$
\tag{55}
$$

$$
\tag{56}
$$

and the fermion-parity term is

$$
\tag{57}
$$

The fermion-parity term is mapped to a single Pauli Z, the same as the Jordan-Wigner transformation.

All stabilizers are mapped to the single Pauli matrix at each horizontal edge, and they can be removed from the system. Next, we check whether the logical operators $U_{\mathrm{JW}} U_e U_{\mathrm{JW}}^{\dagger}$, $U_{\mathrm{JW}} W_f U_{\mathrm{JW}}^{\dagger}$ match the results from the Jordan-Wigner transformation. Essentially, the unitary U_{JW} transforms the local operators of 2d exact bosonization to nonlocal strings for the Majorana hoppings U_e along the vertical direction (edge e is horizontal) while preserving the locality for the Majorana hopping in the horizontal direction (edge e is vertical). Operator $U_{\mathrm{JW}} U_e U_{\mathrm{JW}}^{\dagger}$ for horizontal edges e will pick up a Z string in between, while operator $U_{\mathrm{JW}} U_e U_{\mathrm{JW}}^{\dagger}$ for vertical edges e is the adjacent XX operator. This is precisely the 1d Jordan-Wigner transformation with respect to the ordering chosen in Fig. 23.
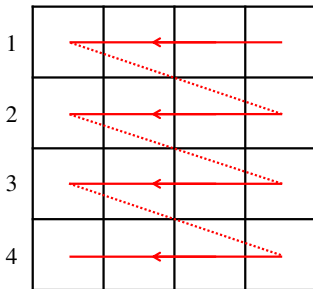

FIG. 23. Ordering of the 1d Jordan-Wigner transformation on the square lattice.

Hence, we can regard the 1d Jordan-Wigner transformation as a particular case in that we remove all the qubits on the horizontal edges where the vertical hoppings are no longer local.

APPENDIX A: CONSTRUCTION OF THE FERMION-TO-QUBIT MAPPING WITH RATIO $r = 1 + 1/l$

In this appendix, we provide an explicit construction of fermion-to-qubit mappings with the qubit-fermion ratio $r = 1 + 1/l$ for any positive integer l. This construction is similar in spirit to the Verstraete-Cirac mapping [3] and the auxiliary qubit mapping [6].

We first specify the Hilbert space, shown in Fig. 24. The square lattice contains red vertices in columns separated by a distance l. For the fermionic Hilbert space, we put one complex fermion at each vertex, generated by operators γ_v, γ_v'. For the bosonic Hilbert space, we put one qubit at each black vertex and two qubits at
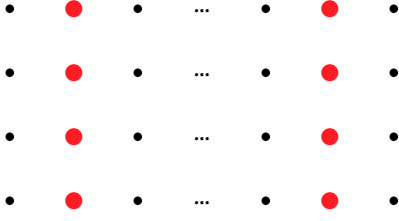
FIG. 24. Physical Hilbert space of the fermion-to-qubit mapping with $r = 1 + 1/l$. Each black site denotes one qubit, and each red site denotes two qubits. Columns of red vertices are separated by a distance l.

each red vertex. We define the mapping between the even sector of the fermionic Hilbert space and the codespace (gauge-invariant subspace) of the bosonic Hilbert space.

The hopping operators on horizontal edges are mapped as

$$\tag{A1}$$

and the operators on vertical edges are

$$\tag{A2}$$

where the vertical hopping operator between black vertices consists of Z-string operators to the nearest red vertices on its right, which has weight $O(l)$. The on-site fermion parity operators at vertices are mapped as

$$\tag{A3}$$

On the bosonic Hilbert space, we need to introduce stabilizers (gauge constraints) to project into the codespace, where the stabilizers are

$$\tag{A4}$$

for each $l \times 1$ rectangle formed by four red vertices, and the "$\cdots$" between the red vertices consist of Z-string operators.

On each $l \times 1$ unit cell, there are l fermions, $l + 1$ qubits, and one stabilizer (gauge constraint), so the degrees of freedom match. The qubit-fermion ratio of this construction is $r = 1 + 1/l$.

APPENDIX B: CLIFFORD GATES

The Clifford group is defined as the group of unitaries that normalize the Pauli group. The Clifford gates are defined as elements in the Clifford group [30,31]. In this paper, we use single-qubit Clifford gates: H gate, S gate, R gate.

The H gate is the Hadamard gate

$$H = \frac{1}{\sqrt{2}} \begin{bmatrix} 1 & 1 \\ 1 & -1 \end{bmatrix} \tag{B1}$$

that satisfies $HXH^\dagger = Z$, $HZH^\dagger = X$. The S gate is the phase gate

$$S = \begin{bmatrix} 1 & 0 \\ 0 & i \end{bmatrix} \tag{B2}$$

that satisfies $SXS^\dagger = Y$, $SYS^\dagger = -X$. The R gate is

$$R = \frac{1}{\sqrt{2}} \begin{bmatrix} 1 & i \\ i & 1 \end{bmatrix} \tag{B3}$$

where $RYR^\dagger = -Z$, $RZR^\dagger = Y$.

For two-qubit Clifford gates, we choose CNOT, CY, and CZ gates. The CNOT gate is

$$\text{CNOT} = \begin{bmatrix} 1 & 0 & 0 & 0 \\ 0 & 1 & 0 & 0 \\ 0 & 0 & 0 & 1 \\ 0 & 0 & 1 & 0 \end{bmatrix}, \tag{B4}$$

where

$$\text{CNOT}(X \otimes I)\text{CNOT}^\dagger = X \otimes X,$$
$$\text{CNOT}(Z \otimes I)\text{CNOT}^\dagger = Z \otimes I,$$
$$\text{CNOT}(I \otimes X)\text{CNOT}^\dagger = I \otimes X,$$
$$\text{CNOT}(I \otimes Z)\text{CNOT}^\dagger = Z \otimes Z.$$

The CY gate is

$$\text{CY} = \begin{bmatrix} 1 & 0 & 0 & 0 \\ 0 & 1 & 0 & 0 \\ 0 & 0 & 0 & -i \\ 0 & 0 & i & 0 \end{bmatrix} \qquad \text{(B5)}$$

where

$$\text{CY}(X \otimes I)\text{CY}^\dagger = X \otimes Y,$$
$$\text{CY}(Z \otimes I)\text{CY}^\dagger = Z \otimes I,$$
$$\text{CY}(I \otimes X)\text{CY}^\dagger = Z \otimes X,$$
$$\text{CY}(I \otimes Z)\text{CY}^\dagger = Z \otimes Z.$$

The CZ gate is

$$\text{CZ} = \begin{bmatrix} 1 & 0 & 0 & 0 \\ 0 & 1 & 0 & 0 \\ 0 & 0 & 1 & 0 \\ 0 & 0 & 0 & -1 \end{bmatrix} \qquad \text{(B6)}$$

where

$$\text{CZ}(X \otimes I)\text{CZ}^\dagger = X \otimes Z,$$
$$\text{CZ}(Z \otimes I)\text{CZ}^\dagger = Z \otimes I,$$
$$\text{CZ}(I \otimes X)\text{CZ}^\dagger = Z \otimes X,$$
$$\text{CZ}(I \otimes Z)\text{CZ}^\dagger = I \otimes Z.$$

APPENDIX C: SUPERCOMPACT MAPPING

In this appendix, we present another representation of the supercompact fermion-to-qubit mapping in Sec. II C. While the supercompact fermion-to-qubit mapping encodes logical fermions on faces, here we discuss another representation that encodes logical fermions on vertices. In this appendix, we show that this mapping encodes logical fermions with $r = 1.25$. On the 2d square lattice in Fig. 25, each black vertex contains a qubit, and each gray vertex contains two qubits. As shown in Figs. 26 and 27, each gray vertex has two Pauli matrices on the top-right and bottom-left corners, respectively. For the encoded information, each vertex v encodes a spinless fermionic mode with creation and annihilation operators $c_v^\dagger$, c_v with the standard commutation relation $\{c_v, c_{v'}^\dagger\} = \delta_{vv'}$ where v denotes the vertex label. The ratio between the number of fermionic modes and the number of physical qubits is 1.25. For convenience, we use the Majorana basis to represent fermionic modes

$$\gamma_v = c_v + c_v^\dagger, \qquad \gamma_v' = \frac{c_v - c_v^\dagger}{i}. \qquad \text{(C1)}$$

The local fermion parity operator at a vertex v is

$$B_v \equiv (-1)^{c_v^\dagger c_v} = -i\gamma_v\gamma_v' \qquad \text{(C2)}$$

and the hopping operator on an edge e is

$$A_{e_{jk}} = i\gamma_j\gamma_k, \qquad \text{(C3)}$$

where j and k are labels for the left and right vertices of edge e. The even algebra of fermions consists of local operators with a trivial fermion parity, i.e., local observables that commute with the total fermion parity $(-1)^F \equiv \prod_v (-1)^{c_v^\dagger c_v}$. The generators for the even algebra of fermions are $A_{e_{jk}}$ and B_v on all edges and vertices [2].

The fermion-to-qubit mappings are mappings from $A_{e_{jk}}, B_v$ to Pauli strings (products of Pauli matrices) on qubits with the same algebra. In addition, such mappings satisfy a condition that the product of $A_{e_{jk}}$ along an arbitrary closed path should be the identity operator (up to a phase) since all Majorana operators cancel out. Such a constraint requires the qubit system to be stabilized by a
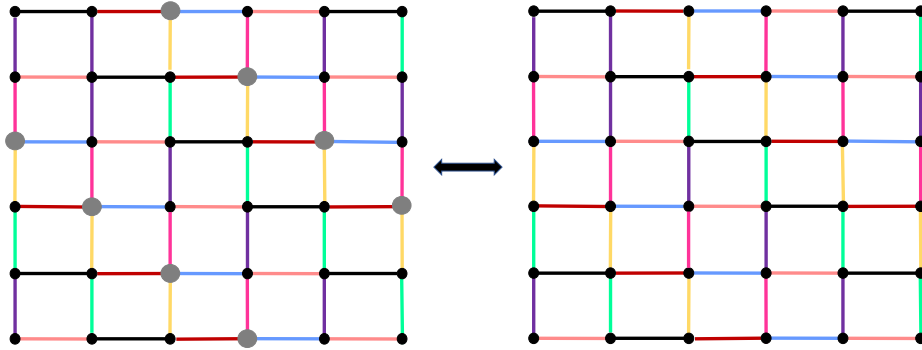

FIG. 25. The physical and logical Hilbert spaces for supercompact encoding. The left-hand side is the physical Hilbert space, where each black vertex contains one qubit, and each gray vertex contains two qubits. The right-hand side is the logical Hilbert space, where each vertex encodes a fermionic mode. The qubit-fermion ratio r is 1.25 in this setting.
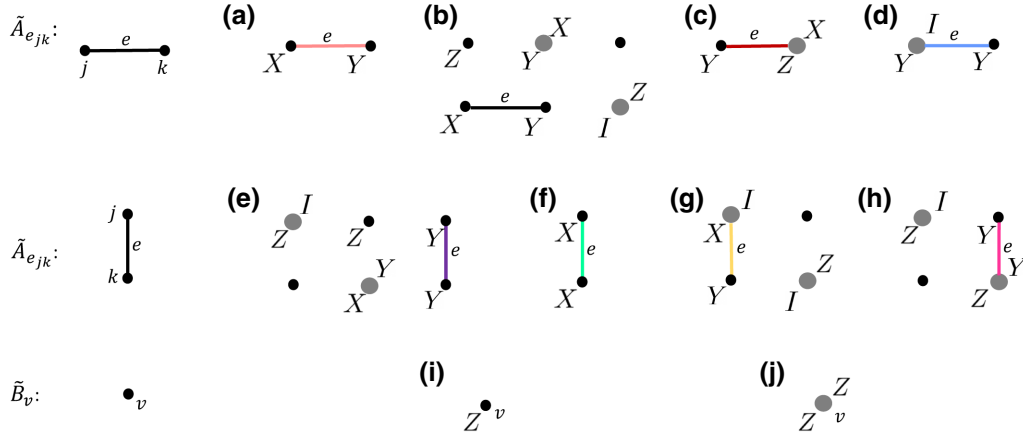
FIG. 26. The hopping term $\tilde{A}_e$ and the parity term $\tilde{B}_v$ in the bosonic Hilbert space. The definitions of $\tilde{A}_e$ and $\tilde{B}_v$ depend on the colors of edges and vertices. (a)–(d) Four kinds of horizontal hopping terms; (e)–(h) four kinds of vertical hopping terms; (i),(j) parity terms on black and gray vertices.

stabilizer group, i.e., being in the $+1$ eigenspace of operators in the stabilizer group. Now, we explicitly construct the mapping on the lattice in Fig. 25:

$$A_{e_{jk}} = i\gamma_j \gamma_k \longleftrightarrow \tilde{A}_{e_{jk}}, \qquad B_v = -i\gamma_v \gamma_v' \longleftrightarrow \tilde{B}_v, \quad (C4)$$

with $\tilde{A}_{e_{jk}}$ and $\tilde{B}_v$ defined in Fig. 26. We may also swap indices j, k for e_{jk}; then we have $A_{e_{kj}} = -A_{e_{kj}} \longleftrightarrow -\tilde{A}_{e_{jk}}$. Since the qubit array has translational symmetries, we color horizontal edges pink, black, brown, and blue, and vertical edges magma, purple, green, and yellow. Hence, there are four different $\tilde{A}_{e_{jk}}$ corresponding to horizontal hoppings along e_{jk} with different colors, and four different $\tilde{A}_{e_{jk}}$ corresponding to vertical hoppings along e_{jk} with different colors. It can be checked that two operators $\tilde{A}_{e_{jk}}$ and $\tilde{A}_{e'_{mn}}$ anticommute if and only if e_{jk} and e'_{mn} are two distinct edges sharing one common vertex, and $\tilde{A}_{e_{jk}}$ and $\tilde{B}_v$ anticommute if and only if edge e contains vertex v. Therefore, $\{A_{e_{jk}}, B_v\}$ and $\{\tilde{A}_{e_{jk}}, \tilde{B}_v\}$ satisfy the same commutation

relations. It is worth noting that we can write all the parity-preserving fermionic operators in a sum of products of $A_{e_{jk}}$ and B_v.

Since the qubit-to-fermion ratio is 1.25, there are stabilizers (gauge constraints) that restrict the qubit array to be in logical subspace. Such constraints are intuitively related to the fact that operators moving a Majorana fermion along a closed loop will be proportional to identity. For a Majorana fermion hopping around a closed loop l, the product of $\tilde{A}_{e_{jk}}$ along l is proportional to the identity operator:

$$\prod_{e_{jk} \in l} \tilde{A}_{e_{jk}} = i^{|l|} \quad (C5)$$

with $|l|$ the length of loop l. This condition comes from the fact that the fermionic operators $A_{e_{jk}}$,

$$\prod_{e_{jk} \in l} A_{e_{jk}} = i^{|l|} \gamma_{l_1} \gamma_{l_2}^2 \cdots \gamma_{l_{|l|}}^2 \gamma_{l_1} = i^{|l|} \gamma_{l_1}^2 = i^{|l|} \quad (C6)$$

which move a Majorana fermion γ along a closed loop l, should be an identity up to a phase factor $i^{|l|}$. Accordingly, the same identity for $\tilde{A}_e$ should also be true on the qubit array; the products of $\tilde{A}_e$ along closed path l should yield the stabilizer (gauge constraints)

$$\prod_{e_{jk} \in l} \tilde{A}_{e_{jk}} = i^{|l|}. \quad (C7)$$

Note that this constraint should be satisfied for all possible closed loops and form a stabilizer group. To encode N fermionic modes, this mapping requires $1.25N$ physical qubits. Hence, there are $0.25N$ stabilizers. The stabilizer generator of this mapping is the operator shown in Fig. 27 that acts on vertices that connect pink, black, green, and
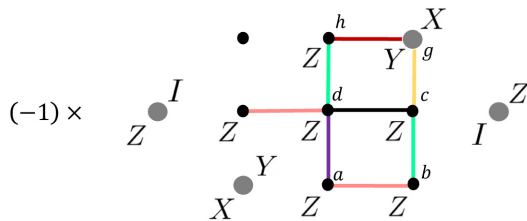

FIG. 27. The stabilizer acts on the vertex d that connects to pink, black, purple, and green edges. This stabilizer comes from identity (C5) for a closed loop $a \rightarrow b \rightarrow c \rightarrow d \rightarrow a$. The product of $\tilde{A}_e$ on any closed loop is generated by this stabilizer.
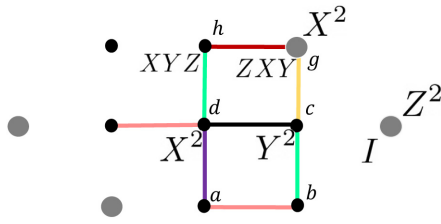
FIG. 28. Stabilizer constraint for the closed loop $d \to c \to g \to h \to d$, which gives $-I$, and it matches identity (C5) on the fermion side $A_{e_{hd}} A_{e_{hg}} A_{e_{gc}} A_{e_{dc}} = -I$.

purple edges. There are $0.25N$ such vertices, so in total there are $0.25N$ stabilizers, as discussed above.

This stabilizer corresponds to Majorana moving along the path $a \to b \to c \to d \to a$. It can be checked that the stabilizer in Fig. 27 commutes with all the logical operators $\tilde{A}_e$, B_v shown in Fig. 26. The weight of such a stabilizer is 12. The logical Hilbert space is the $+1$ eigenspace of this stabilizer that acts on vertices connecting to green, black, purple, and red edges. It is worth noting that the stabilizer shown in Fig. 27 acting on different d can generate all the nontrivial stabilizers where the trivial stabilizers are identity operators. The qubit system should also be stabilized by products of $\tilde{A}_{e_{jk}}$ for other closed loops, and we may wonder whether the product of $\tilde{A}_{e_{jk}}$ along other length-four square loops give nontrivial stabilizers. However, the products of $A_{e_{jk}}$ along other length-four square loops are identity operators. Here we use the square loop $d \to c \to g \to h \to d$ as an example in Fig. 28.

---

[1] For simplicity, we only consider terms respecting the fermion-parity symmetry, i.e., products with even numbers of fermionic creation and annihilation operators. An odd local operator can be constructed by a nonlocal string operator to infinity or a fixed point, analogous to the Jordan-Wigner transformation.

[2] Yu-An Chen, Anton Kapustin, and Djordje Radicevic, Exact bosonization in two spatial dimensions and a new class of lattice gauge theories, Ann. Phys. (N. Y) **393**, 234 (2018).

[3] F Verstraete and J. I. Cirac, Mapping local Hamiltonians of fermions to local Hamiltonians of spins, J. Stat. Mech.: Theory Exp. **2005**, P09012 (2005).

[4] Alexei Kitaev, Anyons in an exactly solved model and beyond, Ann. Phys. (N. Y) **321**, 2 (2006).

[5] James D. Whitfield, Vojtěch Havlíček, and Matthias Troyer, Local spin operators for fermion simulations, Phys. Rev. A **94**, 030301 (2016).

[6] Mark Steudtner and Stephanie Wehner, Quantum codes for quantum simulation of fermions on a square lattice of qubits, Phys. Rev. A **99**, 022308 (2019).

[7] Zhang Jiang, Jarrod McClean, Ryan Babbush, and Hartmut Neven, Majorana Loop Stabilizer Codes for Error

Mitigation in Fermionic Quantum Simulations, Phys. Rev. Appl. **12**, 064041 (2019).

[8] Kanav Setia, Sergey Bravyi, Antonio Mezzacapo, and James D. Whitfield, Superfast encodings for fermionic quantum simulation, Phys. Rev. Res. **1**, 033033 (2019).

[9] Charles Derby, Joel Klassen, Johannes Bausch, and Toby Cubitt, Compact fermion to qubit mappings, Phys. Rev. B **104**, 035118 (2021).

[10] Hoi Chun Po, Symmetric Jordan-Wigner transformation in higher dimensions, (2021), arXiv preprint ArXiv:2107.10842.

[11] Sergey B. Bravyi and Alexei Yu. Kitaev, Fermionic quantum computation, Ann. Phys. (N. Y) **298**, 210 (2002).

[12] Yu-An Chen and Anton Kapustin, Bosonization in three spatial dimensions and a 2-form gauge theory, Phys. Rev. B **100**, 245127 (2019).

[13] Yu-An Chen, Exact bosonization in arbitrary dimensions, Phys. Rev. Res. **2**, 033527 (2020).

[14] Kangle Li and Hoi Chun Po, Higher-dimensional Jordan-Wigner transformation and auxiliary Majorana fermions, Phys. Rev. B **106**, 115109 (2022).

[15] Jacek Wosiek, *A local representation for fermions on a lattice*, Tech. Rep. (institution Univ., Physics Department, 1981).

[16] A. Bochniak and B. Ruba, Bosonization based on Clifford algebras and its gauge theoretic interpretation, J. High Energy Phys. **2020**, 118 (2020).

[17] Arkadiusz Bochniak, Błażej Ruba, Jacek Wosiek, and Adam Wyrzykowski, Constraints of kinematic bosonization in two and higher dimensions, Phys. Rev. D **102**, 114502 (2020).

[18] Arkadiusz Bochniak, Błażej Ruba, and Jacek Wosiek, Bosonization of Majorana modes and edge states, Phys. Rev. B **105**, 155105 (2022).

[19] Lakshya Bhardwaj, Davide Gaiotto, and Anton Kapustin, State sum constructions of spin-tfts and string net constructions of fermionic phases of matter, J. High Energy Phys. **2017**, 96 (2017).

[20] Tyler D. Ellison and Lukasz Fidkowski, Disentangling Interacting Symmetry-Protected Phases of Fermions in Two Dimensions, Phys. Rev. X **9**, 011016 (2019).

[21] Yu-An Chen, Tyler D. Ellison, and Nathanan Tantivasadakarn, Disentangling supercohomology symmetry-protected topological phases in three spatial dimensions, Phys. Rev. Res. **3**, 013056 (2021).

[22] Yu-An Chen and Po-Shen Hsin, Exactly solvable lattice Hamiltonians and gravitational anomalies, (2021), arXiv preprint ArXiv:2110.14644.

[23] Maissam Barkeshli, Yu-An Chen, Sheng-Jie Huang, Ryohei Kobayashi, Nathanan Tantivasadakarn, and Guanyu Zhu, Codimension-2 defects and higher symmetries in (3+ 1) d topological phases, (2022), arXiv preprint ArXiv:2208.07367.

[24] Sergey Bravyi, Barbara M. Terhal, and Bernhard Leemhuis, Majorana fermion codes, New J. Phys. **12**, 083039 (2010).

[25] Sagar Vijay and Liang Fu, Physical implementation of a Majorana fermion surface code for fault-tolerant quantum computation, Phys. Scr. **2016**, 014002 (2016).

[26] Oscar Viyuela, Sagar Vijay, and Liang Fu, Scalable fermionic error correction in Majorana surface codes, Phys. Rev. B **99**, 205114 (2019).

[27] Sagar Vijay, Timothy H. Hsieh, and Liang Fu, Majorana Fermion Surface Code for Universal Quantum Computation, Phys. Rev. X **5**, 041038 (2015).

[28] Daniel Litinski and Felix von Oppen, Quantum computing with Majorana fermion codes, Phys. Rev. B **97**, 205404 (2018).

[29] M. B. Hastings, Small Majorana fermion codes, (2017), ArXiv:1703.00612.

[30] Daniel Gottesman, Theory of fault-tolerant quantum computation, Phys. Rev. A **57**, 127 (1998).

[31] Daniel Gottesman, The Heisenberg representation of quantum computers, (1998), arXiv preprint ArXiv:9807006.

[32] Xie Chen, Zheng-Cheng Gu, and Xiao-Gang Wen, Local unitary transformation, long-range quantum entanglement, wave function renormalization, and topological order, Phys. Rev. B **82**, 155138 (2010).

[33] Bei Zeng, Xie Chen, Duan-Lu Zhou, and Xiao-Gang Wen, Quantum information meets quantum matter – from quantum entanglement to topological phase in many-body systems, (2018), ArXiv:1508.02595.

[34] Michael Freedman and Matthew B. Hastings, Classification of quantum cellular automata, Commun. Math. Phys. **376**, 1171 (2020).

[35] Jeongwan Haah, Clifford quantum cellular automata: Trivial group in 2D and Witt group in 3D, J. Math. Phys. **62**, 092202 (2021).

[36] Daniel Gottesman, *Stabilizer Codes and Quantum Error Correction* (California Institute of Technology, Pasadena, 1997).

[37] The logical operators consist of all operators commuting with the stabilizer Hamiltonian. The logical operators preserve the codespace, i.e., mapping codewords from one to another.

[38] Substituting the definitions of P_f and S_e into Eqs. (8) and (9), $P_a P_c S_{e_{58}} S_{e_{56}} S_{e_{25}} S_{e_{45}}$ is equal to $\gamma_a^2 \gamma_a'^2 \gamma_b'^2 \gamma_c^2 \gamma_c'^2 \gamma_d^2$, which is the identity due to the property of Majorana fermions.

[39] The logical operators consist of all operators that commute with $\mathcal{G}$. The $\mathcal{G}$ are trivial logical operators since stabilizers do not affect the codespace. Operators U_e and W_f generate all logical operators.

[40] Nicolas Tarantino and Lukasz Fidkowski, Discrete spin structures and commuting projector models for two-dimensional fermionic symmetry-protected topological phases, Phys. Rev. B **94**, 115115 (2016).

[41] Qing-Rui Wang and Zheng-Cheng Gu, Towards a Complete Classification of Symmetry-Protected Topological Phases for Interacting Fermions in Three Dimensions and a General Group Supercohomology Theory, Phys. Rev. X **8**, 011055 (2018).

[42] Qing-Rui Wang and Zheng-Cheng Gu, Construction and Classification of Symmetry-Protected Topological Phases in Interacting Fermion Systems, Phys. Rev. X **10**, 031055 (2020).

[43] The portion of gray faces over all faces is $1/2k$. After removing stabilizers on white faces, the qubit-fermion ratio becomes $r = 1 + 1/2k$.

[44] Jeongwan Haah, Lukasz Fidkowski, and Matthew B. Hastings, Nontrivial quantum cellular automata in higher dimensions, Commun. Math. Phys. (2022),.

[45] The "potential" flipper is an operator satisfying algebra (29) partially. For example, it may anticommute with extra separators $\tilde{Z}_{e'}$. This issue can be fixed by attaching other operators to this potential flipper.

[46] To be precise, we consider the mapping between local fermionic observables and local products of Pauli matrices.

[47] Jeongwan Haah, Classification of translation invariant topological Pauli stabilizer codes for prime dimensional qudits on two-dimensional lattices, J. Math. Phys. **62**, 012201 (2021).

[48] In this paper, we only work on qubits, which corresponds to $p = 2$. Therefore, the theorem in Ref. [47] is valid.

[49] There are other symmetrical ways to incorporate the spins by considering two layers of toric codes with one spin up and one spin down, i.e., a thin slab of the 3D bosonization [12], or by choosing another representation of Pauli matrices locally [10]. We can always project these constructions onto a 2D surface and apply the argument above.

[50] The relative ordering between two edges e and e' determines either $e < e'$ or $e > e'$. The transitive relation is not required, i.e., possibly $e < e'$, $e' < e''$, and $e'' < e$.

[51] Here the edge effect is ignored since we work on a translationally invariant system.

[52] The depth of the circuit scales linearly with the system size.